

In-plane and out-of-plane excitonic coupling in 2D molecular crystals

Received: 12 August 2022

Accepted: 17 April 2023

Published online: 12 May 2023

 Check for updatesDogyeong Kim¹, Sol Lee^{2,3}, Jiwon Park¹, Jinho Lee¹, Hee Cheul Choi¹,
Kwanpyo Kim^{2,3} & Sunmin Ryu¹✉

Understanding the nature of molecular excitons in low-dimensional molecular solids is of paramount importance in fundamental photophysics and various applications such as energy harvesting, switching electronics and display devices. Despite this, the spatial evolution of molecular excitons and their transition dipoles have not been captured in the precision of molecular length scales. Here we show in-plane and out-of-plane excitonic evolution in quasi-layered two-dimensional (2D) perylene-3, 4, 9, 10-tetracarboxylic dianhydride (PTCDA) crystals assembly-grown on hexagonal boron nitride (hBN) crystals. Complete lattice constants with orientations of two herringbone-configured basis molecules are determined with polarization-resolved spectroscopy and electron diffraction methods. In the truly 2D limit of single layers, two Frenkel emissions Davydov-split by Kasha-type intralayer coupling exhibit energy inversion with decreasing temperature, which enhances excitonic coherence. As the thickness increases, the transition dipole moments of newly emerging charge transfer excitons are reoriented because of mixing with the Frenkel states. The current spatial anatomy of 2D molecular excitons will inspire a deeper understanding and groundbreaking applications of low-dimensional molecular systems.

Excitons in molecular solids mediate efficient light harvesting in photosynthesis complexes¹ and important organo-electronic applications such as photovoltaics² and light-emitting diodes³. They also present a myriad of intriguing photophysical phenomena such as Davydov splitting (DS)^{4,5} associated with J/H aggregates⁶, coherence-induced superradiance⁷, mixing of Frenkel and charge-transfer⁸ excitons⁹, and singlet fissions¹⁰. Despite their small footprints spanning a few unit cells, molecular excitons are greatly affected by intermolecular interactions through Kasha-type Coulombic¹¹ and intermolecular CT¹² couplings. Geometric arrangements are crucial in both interactions in that the former is governed by the long-range coupling among transition dipoles¹³, whereas the latter is by the short-range orbital overlap¹⁴. Notably, the CT coupling is ubiquitous in π -stacked systems, differentiates the J/H-aggregate behaviors¹⁵, limits the coherence of Frenkel excitons (FE)^{16,17}, and facilitates the singlet fission¹⁸. Despite many experimental breakthroughs and progress¹⁹, however, it remains

unclear how the evolution of Frenkel-CT mixing can be revealed by other than differing energetics^{20–22}. By exploiting the capability of polarized spectroscopy that directly maps the transition dipoles, more direct proof for the mixing and its spatial progression should be within experimental reach.

For such an exploration, two-dimensional molecular crystals (2DMCs) can be an ideal system^{23,24}. In principle, the above interactions can be tuned by varying intermolecular arrangements, dielectric environments, and the extent of coupled units. In bulk crystals, however, the two former parameters are thermodynamically fixed and can hardly be modified except for polymorphic transitions. Whereas the number of molecular units under excitonic coupling can be purposefully varied by forming oligomers with chemical bonds²⁵, it is not applicable to the molecular crystals formed via van der Waals (vdW) interactions, either. In contrast, variable-thickness 2DMCs epitaxially grown on crystalline templates can provide crucial controls over the

¹Department of Chemistry, Pohang University of Science and Technology (POSTECH), Pohang, Gyeongbuk 37673, Korea. ²Department of Physics, Yonsei University, Seoul 03722, Korea. ³Center for Nanomedicine, Institute for Basic Science (IBS), Seoul 03722, Korea. ✉e-mail: sunryu@postech.ac.kr

geometric factors. Most of all, the crystalline structure of 2DMCs is affected by the templates, which may enable customizing intermolecular geometry^{24,26}. Monolayer-resolved thickness control will allow fine-tuning of the spatial extent of excitonic coupling²⁷ and the degree of dielectric screening²⁸. The distinction between in-plane and out-of-plane couplings may also be made by varying thickness approaching the truly 2D limit.

In this work, we directly reveal the in-plane and out-of-plane excitonic evolutions of 2D PTCDA (perylene-3,4,9,10-tetracarboxylic dianhydride) crystals grown on hexagonal BN (hBN) substrates in an unprecedented manner using polarized photoluminescence (PL) and absorption spectroscopies. The crystalline structure of PTCDA and its epitaxial registry with hBN were revealed by electron diffractions. The excitons confined within monolayer PTCDA exhibited enhanced in-plane coherence and superradiance at cryogenic temperatures, which was supported by the inversion in DS. We also show that PL from CT excitons is dominant in multilayer PTCDA and their transition dipoles are drastically reoriented with increasing thickness as a result of varying CT contribution in Frenkel-CT mixing. The anatomy of the excitonic couplings in 2D PTCDA shown in this work can be applied to other 2DMCs and serve as a touchstone for the theoretical modeling of Frenkel-CT interactions.

Results and discussion

Structural and optical characterization of 2D PTCDA crystals

Single and few-layer 2D PTCDA crystals (nL_P) shown in Fig. 1a were grown on few-layer hBN (nL_{BN}) by physical vapor deposition (PVD) at elevated temperatures. The AFM height image (Fig. 1a) and profile (Fig. 1b) showed a flat layered structure with an interlayer spacing of 0.31 ± 0.08 nm (more examples with optical micrographs are given in Supplementary Fig. 1). As described in Methods, crystalline substrates for growth and excess thermal energy^{23,24} were crucial in obtaining ordered structures. The crystalline nature of the samples was revealed by electron diffraction, as shown in the selected area electron diffraction (SAED) image of $2L_G/1L_P/nL_{BN}$ (Fig. 1c), where the encapsulation with bilayer graphene ($2L_G$) led to greatly enhanced stability against electron-induced damages (see Methods). Analysis of multiple samples verified that the rectangular unit cell determined by the diffraction method corresponds to (102)-plane unit cell of bulk crystals²⁹. Then, m and n spanning the 2D unit cell (Fig. 1d) are equivalent respectively to b and $[\bar{2}01]$ of bulk: $m = 1.256 \pm 0.018$ (1.220 ± 0.030) nm, $n = 1.971 \pm 0.017$ (1.972 ± 0.008) nm for $1L_P$ ($3L_P$). As summarized in Supplementary Table 1, m of $1L_P$ was -6% longer than that of bulk³⁰, but the deviation was reduced for $3L_P$, which suggests convergence toward the bulk value with increasing thickness. In addition, the fact that interlayer spacing in 2D PTCDA is very close to that of bulk³⁰

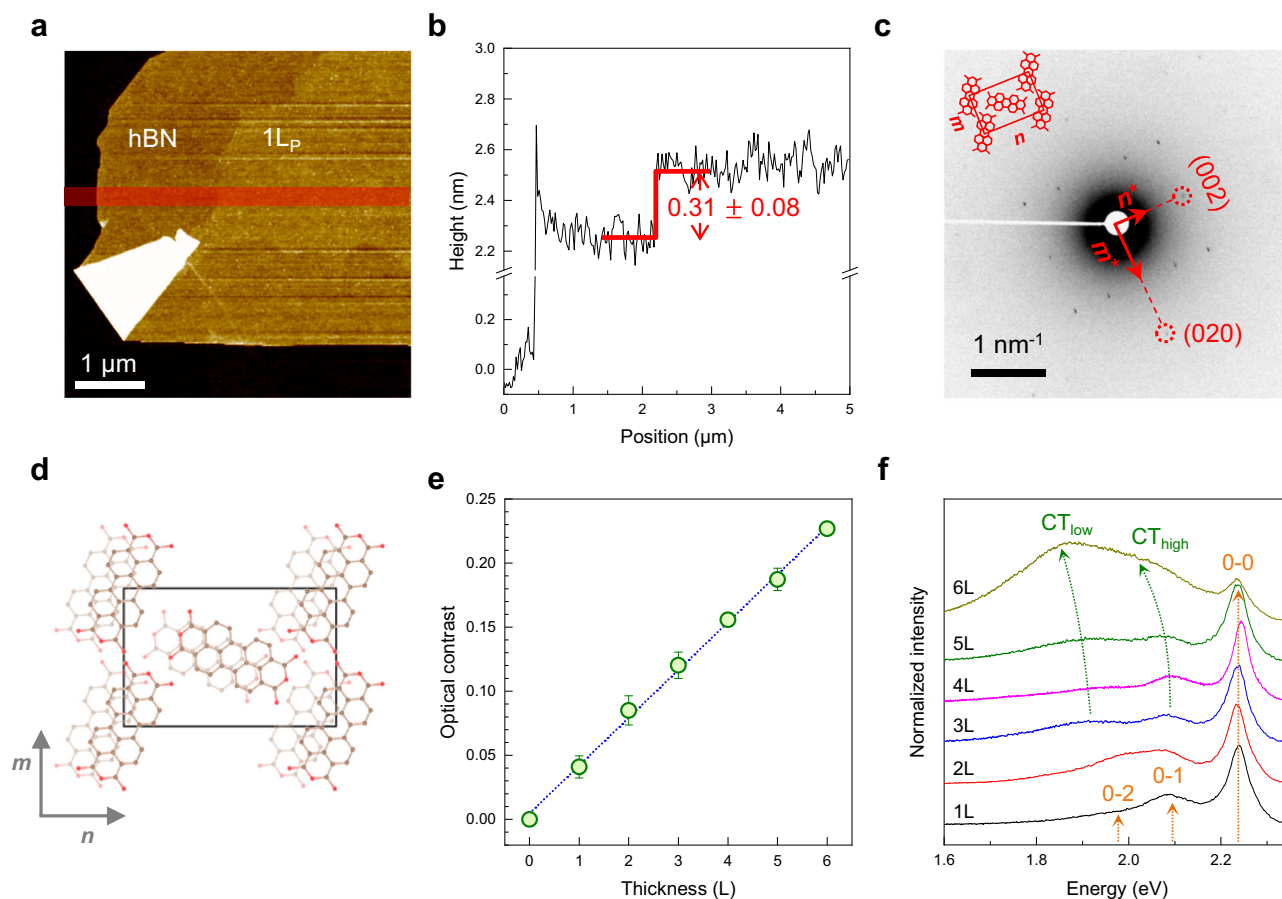


Fig. 1 | Structural and optical characterization of 2D PTCDA crystals. **a** AFM height image of $1L_P$ on few-layer hBN/SiO₂/Si (see Supplementary Fig. 1 for its optical micrographs before and after PVD). **b** Averaged height profile obtained in the red area in **a**. **c** SAED image from $2L_G/1L_P/nL_{BN}$, where $2L_G$ served as a protection layer (see Methods and Supplementary Fig. 12 for details). The optical micrograph of the assembled heterostructure is given in Supplementary Fig. 2. The inset presents a schematic two-basis unit cell of $1L_P$ crystals determined by electron diffraction and polarized PL spectroscopy, where unit vectors m and n correspond to b and $[\bar{2}01]$ of bulk crystals. The real-space orientation of the unit cell, rectangle in

d, was determined by the reciprocal vectors (m^* and n^*) of diffraction images. **d** Proposed structure of $2L_P$ crystals resembling α -type polymorph with two-basis molecules in a herringbone configuration. The molecules in pale colors belong to the bottom layer. **e** Optical contrast of $1L_P$ - $6L_P$ on hBN/quartz determined using the green-channel signals of optical micrographs. The dashed line is a linear fit to the data. Error bars indicate standard deviations obtained from multiple samples. **f** Unpolarized PL spectra of $1L_P$ - $6L_P$ on hBN. See the text for the assignment of various PL peaks.

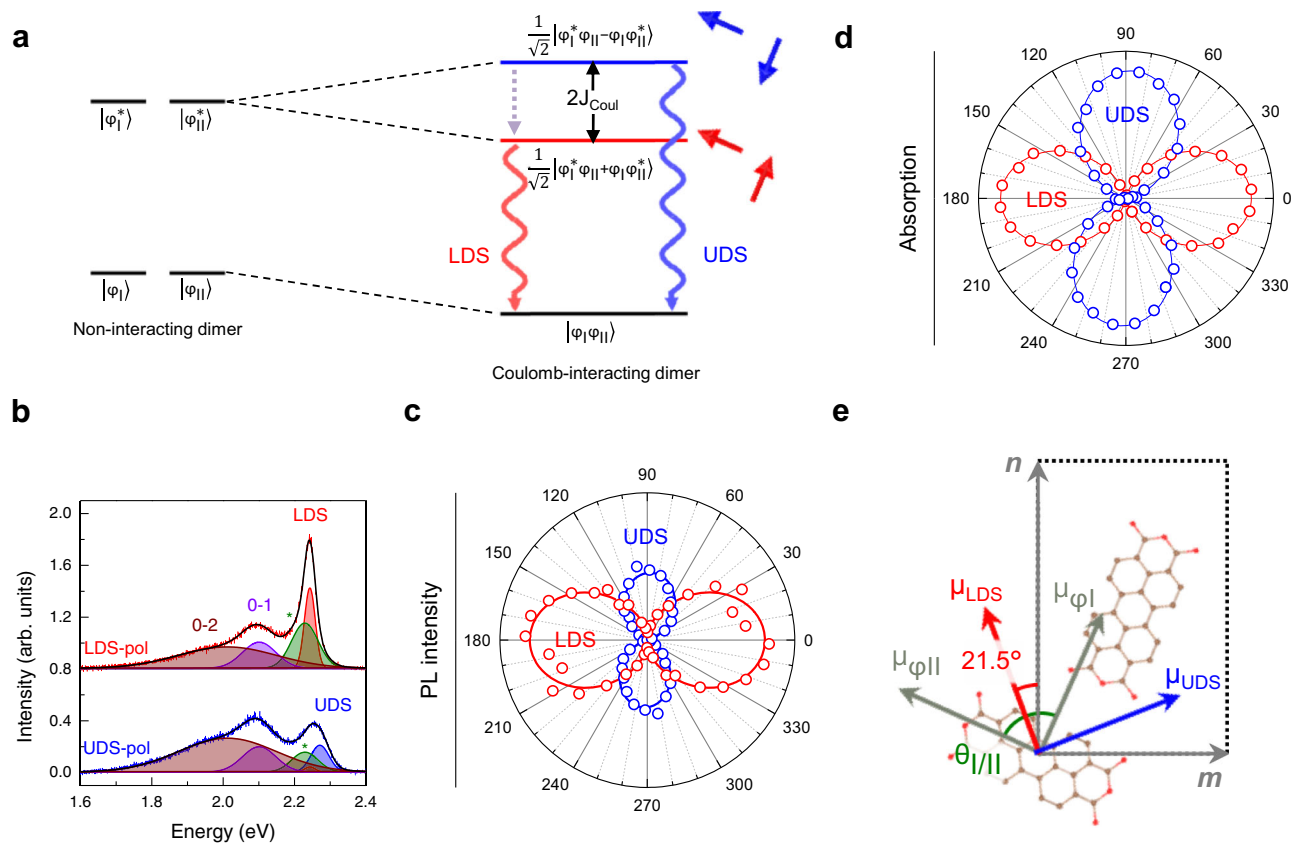


Fig. 2 | Optical anisotropy and epitaxial growth of 1L PTCDA. **a** Scheme of Davydov splitting in an oblique PTCDA dimer described by ground (φ_i) and excited-state wavefunctions (φ_i^*). LDS and UDS are the superpositions of φ_i and φ_i^* resulting from the Coulombic interactions (J_{Coul}) between molecular transition dipoles (oblique arrows). **b** LDS and UDS-polarized PL spectra of 1L_P on hBN obtained in a parallel configuration, where the polarizations of the excitation beam and PL signals were aligned with μ_{LDS} (upper) and μ_{UDS} (lower), respectively. Complete sets of spectra (Supplementary Fig. 5) were globally fitted with multiple Gaussian functions for 0-*v*

vibronic components, where *v* refers to the vibrational quantum number of the electronic ground state and the pair of LDS and UDS corresponds to the 0-0 transition. The origin of the peak at 2.21 eV (marked with asterisks) is unclear. **c** Polar graph of PL intensity for LDS and UDS peaks, where the data were fitted with the square of cosine. **d** Polar graph of differential reflectance (DR) for LDS and UDS peaks, for the latter of which an angle-independent constant was subtracted (see Supplementary Fig. 2 for complete DR spectra). **e** Orientations of molecular and DS transition dipole moments determined with polarized spectroscopy and electron diffraction.

corroborates that 1L_P corresponds to a single (102) plane²⁹. As shown below, DS in PL spectra indicated that two-basis molecules are arranged in a herringbone configuration as in bulk crystals³⁰. The orientation of each basis molecule within the unit cell could be determined by polarization-resolved absorption spectra as described in Supplementary Fig. 2. The simulated diffraction pattern in Supplementary Fig. 3 also showed that 2D PTCDA is closer to the α polymorph, preferred for higher growth temperature, rather than β ³¹ (see Supplementary Fig. 4 for their structural difference). Note that the unit cells in two neighboring layers are displaced against each other along n as depicted in Fig. 1d. The formation of the 2D crystalline layered structure is assisted by the interplanar π - π interaction^{32,33} and in-plane hydrogen bonding³⁴. We also note there is a specific orientational registry between nL_P and underlying hBN: the n axis of 1L_P and 3L_P formed $10.6 \pm 0.1^\circ$ with the armchair direction of hBN (Supplementary Fig. 3h). This indicates that the crystalline nature of 2D PTCDA is supported by substrate-mediated epitaxial growth. In contrast, graphene allows two different rotational polytypes (Supplementary Fig. 3b, c). More restrictive binding on hBN than graphene was also reported for tetracene molecules²⁴.

In addition to the topographic measurements, the average thickness of PTCDA samples could be determined by optical contrast (Methods), which is proportional to the degree of absorption for thin samples supported on transparent substrates³⁵. Figure 1e showed a good resolution for thickness and linearity up to 6 layers. The spectral changes in the room-temperature PL spectra (Fig. 1f) were largely

consistent with previous studies on bulk crystals and thin films:^{32,33} whereas monolayer samples present localized FEs with a substantial vibronic progression, thicker samples are dominated by CT excitons denoted as CT_{high} and CT_{low}, which are coupled with lattice phonons to varying degrees^{32,33}. CT excitons have been modeled to reside in 1D molecular stacks under the assumption that the in-plane excitonic coupling is negligible compared to the interplanar π - π interactions^{9,20,36}. Although the low-energy PL peaks are mostly of the CT-exciton character^{9,32}, the exact nature and assignment of each peak is far from reaching a consensus^{32,33}. We note that a systematic study is required to relate the current CT_{high} and CT_{low} of few-layer PTCDA with those found for bulk samples.

Davydov splitting and in-plane excitonic coupling of 1L PTCDA crystals

The bulk-like rectangular unit cell determined by the diffraction measurements suggests that each unit cell contains two-basis molecules hydrogen-bonded in a herringbone configuration of α polymorph³⁰ (Supplementary Fig. 3). According to Kasha's dimer model¹¹, the FE state of a two-basis system undergoes DS and splits into two states in general. As depicted in Fig. 2a, the Coulomb interaction (J_{Coul}) converts the degenerate excited states of a non-interacting dimer (denoted as φ_i and φ_{ii}) into the lower and upper DS states, denoted as LDS and UDS, respectively. The two DS states can be described as the symmetric and antisymmetric superposition of φ_i^*

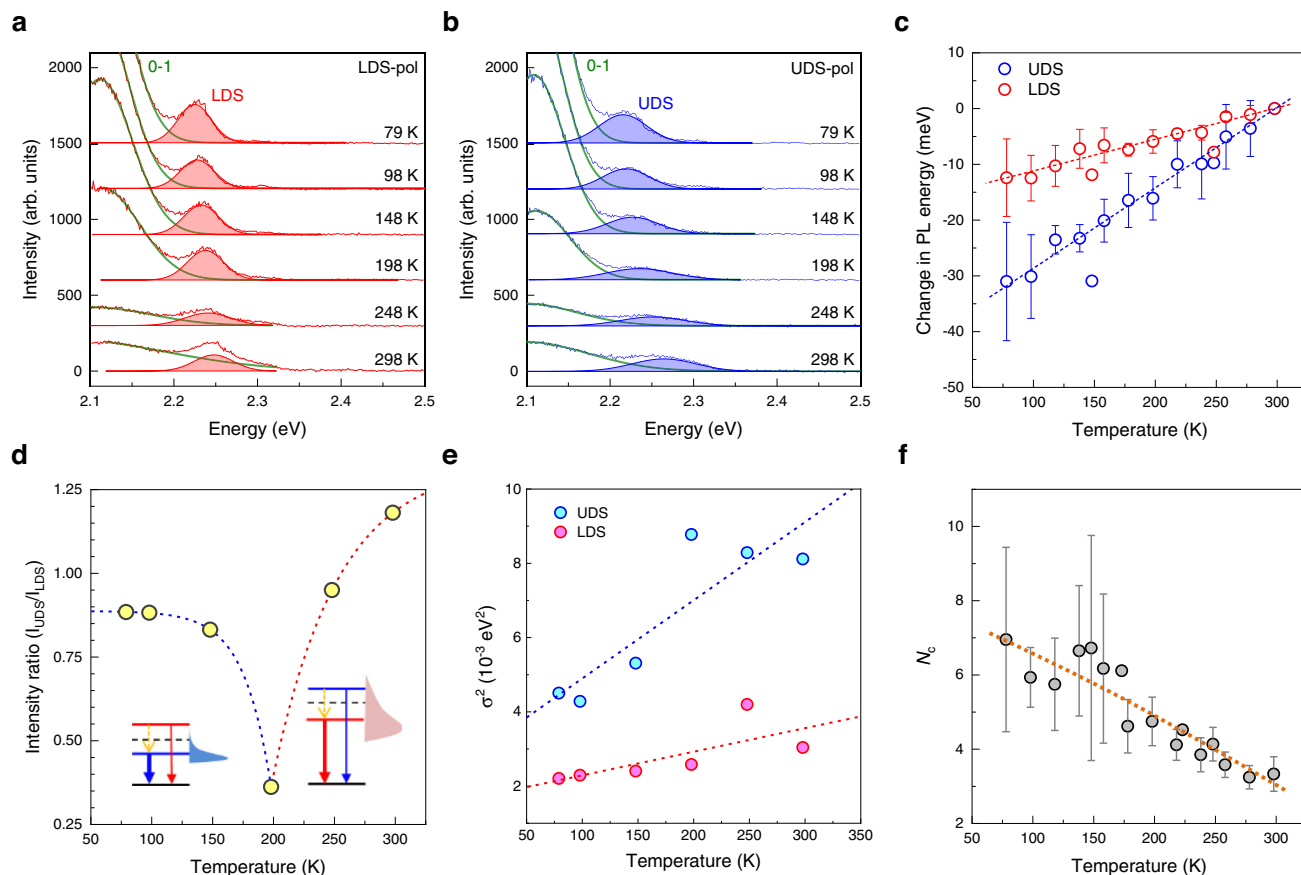


Fig. 3 | Temperature-dependent Davydov splitting. **a, b** Polarized PL spectra of 1L_P/hBN: LDS- (**a**) and UDS-polarized (**b**) spectra obtained for 79–298 K. Each spectrum in **a, b** was fitted with two Gaussian functions for 0–0 and 0–1 peaks. Note that the unknown peak at 2.2 eV identified in Fig. 2b was not included in the fitting because of the lack of sufficient spectra required for a global analysis. **c** Change in PL energy when referenced at 298 K. **d, e** Intensity ratio (**d**) and FWHM squared σ^2 (**e**) of LDS and UDS peaks. The scheme in **d** depicts an energy inversion in DS and

the associated change in Boltzmann-type populations with decreasing temperature. **f** Coherence number (N_c) of 1L_P determined by comparing linewidths following: $N_c = \sigma_{\text{mono}}^2 / \sigma_{2D}^2$ and $N_c \propto 1/T^{5/2}$, where σ_{mono} (σ_{2D}) is FWHM of 0–0 peaks for monomeric (2D) PTCDA and T is temperature, respectively. PL spectra of monomeric solutions are given in Supplementary Fig. 8. Dotted lines in **c** and **e** are linear fits, whereas those in **d** and **f** are guides to the eye. Error bars in **c** and **f** indicate standard deviations obtained from multiple samples.

and φ_{II} . Under a point-dipole approximation, the split energy (E_{DS}) corresponding to $2J_{\text{Coul}}$ will be governed by mutual orientations and displacement between the two transition dipole moments that are represented by the red (blue) arrow pairs in Fig. 2a. Their transition dipole moments (μ_{LDS} and μ_{UDS}) are expected to be orthogonal to each other, no matter what angle the transition dipole moments of the two bases ($\mu_{\varphi I}$ and $\mu_{\varphi II}$) form⁵. To determine the orientations of the DS dipoles, we obtained polarized PL spectra of 1L_P in a parallel configuration by rotating excitation polarization (see Supplementary Fig. 5 for a complete set of spectra). In Fig. 2b presenting LDS and UDS-polarized spectra, the 0–0 transition led to two prominent DS peaks with E_{DS} of 36 meV. Their polar intensity graph in Fig. 2c verified their orthogonality (90.2 ± 1.3 deg for multiple samples). UDS still showed significant signals at the intensity minimum unlike LDS, the origin of which is not clear. The DS of 0–1 and 0–2 peaks could not be discerned because of their large spectral widths and overlap. Notably, the DS has not yet been observed in any form of PTCDA solids directly by emission or absorption spectroscopy. In addition to the lacking availability of single crystals of sufficient quality and size, dominant CT emission³⁷ and extremely high absorption³⁸ impede the conventional polarized measurements, respectively. The only experimental E_{DS} , 37 meV for α -PTCDA, was determined by ellipsometry³⁸.

Correlated measurements of electron diffraction and polarized PL (Supplementary Fig. 2) allowed us to determine the orientation of μ_{LDS} and μ_{UDS} with respect to the crystallographic coordinates of 2D

PTCDA. As shown in Fig. 2e for 1L_P, μ_{LDS} was found to make an angle of 21.5° with the \mathbf{n} axis. We note that this information can be used in determining the molecular orientation in 2D PTCDA because molecular transition dipoles are aligned along the long molecular axis¹⁷. Assuming that $\mu_{\varphi I}$ and $\mu_{\varphi II}$ are identical in their magnitudes, μ_{LDS} (μ_{UDS}) is parallel (perpendicular) to the bisector of the angle ($\theta_{I/II}$) formed by $\mu_{\varphi I}$ and $\mu_{\varphi II}$ (Fig. 2e). As $\theta_{I/II}$ governs the relative magnitude of the DS dipoles, it could be determined by comparing the absorption by LDS and UDS (see Supplementary Fig. 2 for details). The scheme in Fig. 2e depicts the molecular arrangement of 1L_P determined by the diffraction, polarized PL, and absorption measurements. The fact that $\theta_{I/II} = 89.2^\circ$ indicates that the two bases are aligned almost perpendicularly to each other, unlike bulk crystals with $\theta_{I/II} = 96^\circ$ ²⁹.

In Fig. 3, we show a distinctive temperature dependence of the DS peaks of 1L_P. Whereas the emission from UDS (LDS) of J (H) dimers is dipole-forbidden¹¹, both DS transitions of oblique dimers found in 2D PTCDA and tetracene²⁴ are allowed. Because of rapid internal conversion³⁹, the emission from UDS is insignificant unless E_{DS} is close to or smaller than the thermal energy like PTCDA (Fig. 2a). For example, 2D tetracene showed negligible UDS intensity because of its large E_{DS} (~ 95 meV) which hinders the thermal population of UDS²⁴. The two sets of polarized PL spectra of 1L_P (Fig. 3a, b) clearly show that LDS and UDS redshift with decreasing temperature. Remarkably, the rate of redshift is 2.7 times larger for UDS than LDS as shown in Fig. 3c (see

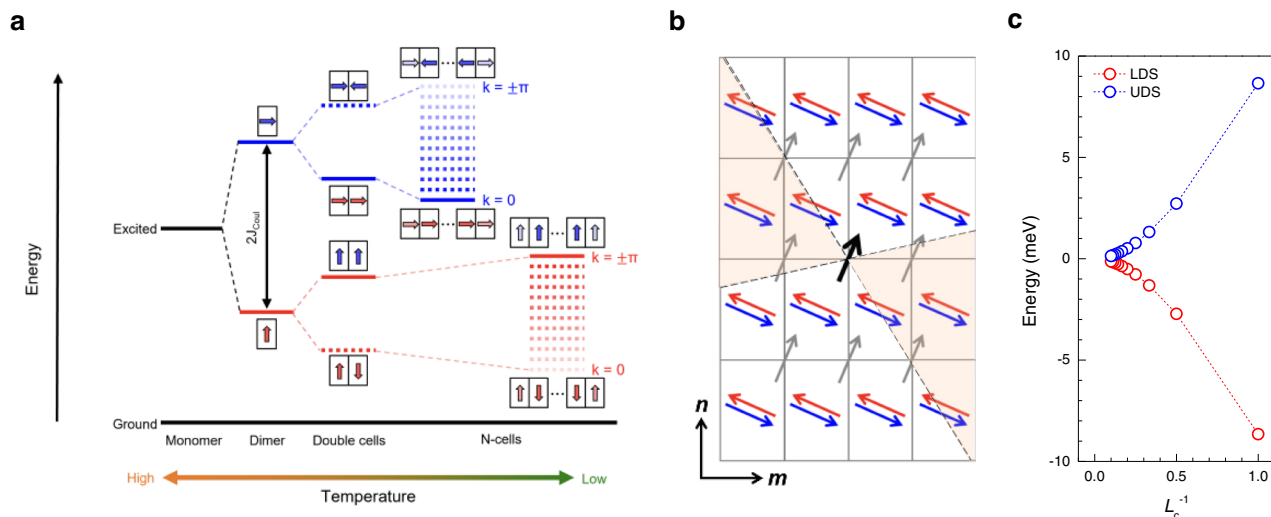


Fig. 4 | Extended 2D excitonic coherence at low temperature. **a** Excitonic progression in 1D molecular crystals with increasing coherence. For a dimer represented by a unit cell (black rectangle), the Coulomb interaction (J_{Coul}) between two molecular bases (I and II) leads to the LDS (red arrows) and UDS (blue arrows) dipoles. For simplicity, the LDS and UDS dipoles are set parallel to one of the unit cell edges. With decreasing temperature, more DS dipoles undergo coherent coupling, which can be approximated as the double-cell and N-cell cases in **a**. The delocalized coupling leads to excitonic bands for LDS (red dotted band) and UDS (blue dotted band). Only the uppermost (lowermost) state is optically accessible for the LDS (UDS) band, where k represents the crystal momentum. **b** 2D arrangement of molecular transition dipoles determined for 1L_P and used for the

electrostatic calculations shown in **c**. Four type-II dipoles (red and blue arrows) in the first shell of the reference dipole at the center (black arrow; type-I) orient in opposite directions for LDS (red arrows) and UDS (blue arrows) coupling, whereas all type-I dipoles including eight in the second shell (gray arrows) remain unchanged. Type-I dipoles in the two orange quadrants interact repulsively with the reference dipole. **c** Energy of the reference transition dipole moment interacting with another delocalized over neighboring type-II dipoles. Coherence length⁴⁵ is defined as the number of type-II shells surrounding the reference dipole: the first and second shells contain 4 and 12 type-II dipoles, respectively. We used 6.93 Debye for the monomeric transition dipole moment⁶¹ and $\epsilon = 1$ for simplicity.

Supplementary Fig. 6 for more data and Supplementary Fig. 7 for complete spectra), which leads to the inversions in the peak energies (Supplementary Fig. 7) and intensity ratio (Fig. 3c, d). The spectral narrowing (Fig. 3e) accompanied by the increase of their intensities suggests that their excitonic decay is mainly governed by superradiance⁴⁰, an accelerated spontaneous emission from coherently coupled⁴¹ or delocalized⁴² excitons. The degree of delocalization will be discussed later using the molecular coherence number, N_c (Fig. 3f), which was extracted from the linewidth (σ)⁴³.

The temperature dependence of both DS peaks in Fig. 3 provides a crucial insight into the nature of excitonic coupling in 1L_P. According to Kasha's exciton model¹¹, the excited state of a herringbone-configured PTCDA dimer splits into LDS and UDS (Fig. 4a), and their average energy is slightly lower than that of the excited monomer. The former is induced by the Coulombic interaction between two transition dipoles, whereas the latter is due to differing vdW interaction between ground-state and excited molecules. The long-range Coulombic interaction can be further extended to 1D arrays of unit cells containing two bases, where the number of unit cells represents the degree of exciton delocalization. For example, the inter-dipole interaction will split LDS and UDS into two states for double cells and N states for N cells (Fig. 4a). Because only the uppermost (lowermost) state is optically allowed for the LDS (UDS) band¹¹, the optical transition energy increases (decreases) for LDS (UDS) with increasing N. As excitons are more delocalized at a lower temperature because of reduced phonon-induced dephasing⁸, the prediction in Fig. 4a is qualitatively consistent with the differing shift rates of the DS peak energies (Fig. 3c). For a more realistic description, one may need to consider the influence of structural disorder that can be present in samples. Disorder limits the degree of delocalization and induces a redshift in excitonic states under short-range potential fluctuations⁴⁴.

To account for the long-range Coulombic interaction among transition dipole moments of excitons delocalized in 2D crystals, we performed a simple electrostatic calculation under the point-dipole

approximation¹¹. Using the structural information revealed by the diffraction and polarized spectroscopy, 2D arrays of transition dipoles for 1L_P were generated as schematically given in Fig. 4b. The reference dipole (black arrow; basis I) at the center interacts attractively and repulsively with four type-II bases (first-shell neighbors) under LDS (red arrow) and UDS (blue arrow) coupling, respectively. Figure 4c shows that the energy for UDS (LDS) coupling decreases (increases) with increasing the number of interacting dipoles represented by the coherence length⁴⁵, which is defined as the number of type-II shells interacting with the reference dipole in Fig. 4b. As L_c is equivalent to length, it is proportional to $N_c^{1/2}$. We note that UDS is stabilized by -10 meV when L_c increases sufficiently and this value is one-third of the change in UDS energy as temperature decreased from 298 K to 77 K (Fig. 3c). The opposite L_c -dependences of LDS and UDS captured in Fig. 3c provides a qualitative justification for the observed energy inversion despite the limitations of the simple model. Quantitative description can be obtained by considering exciton-phonon interactions⁴⁶ and non-dipolar short-range interactions⁴⁵.

We note that the significant redshift found for 2D PTCDA differs from the behavior of bulk polyacene crystals⁴⁷. Negligibly small temperature dependence of the excitonic energy of the bulk system is due to the almost complete cancellation of two competing factors: thermal expansion and exciton-phonon coupling⁴⁷. The sole contribution of the former is also insignificant for the current system assuming compliant thermal expansion: despite its negative thermal expansion coefficient (TEC)⁴⁸, few-nm-thick hBN shrinks with decreasing temperature when supported on amorphous quartz substrates with positive TEC because hBN complies with the thermal expansion of underlying substrates because of the vdW bonding between the two⁴⁹. Similarly, 2D PTCDA is likely to comply with hBN because of their epitaxial registry. Then, the TEC of amorphous quartz predicts that the substrate-induced thermal expansion of 2D PTCDA by cooling from 298 to 79 K is $< -0.02\%$ ⁵⁰, for which many-body calculations⁴⁷ predicted sub-meV redshift for polyacene molecular crystals. In case 2D PTCDA

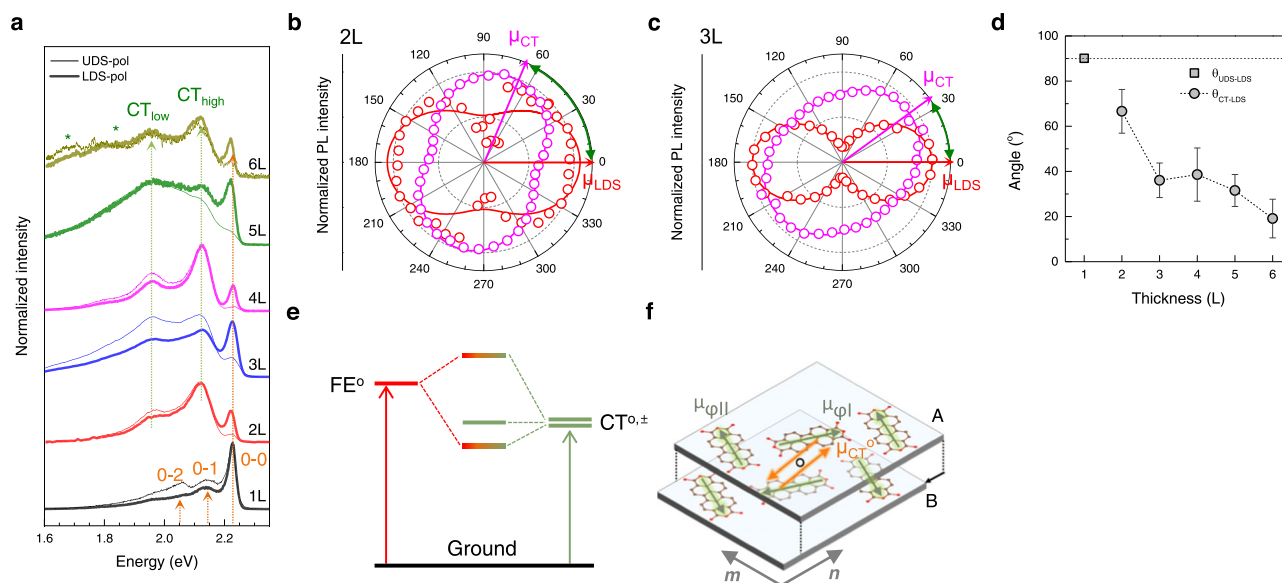


Fig. 5 | Spatial reorientation of CT excitons with varying thickness. **a** LDS- and UDS-polarized PL spectra of nL_P on hBN obtained at 77 K. For the asterisk-marked peaks below 1.9 eV, see Supplementary Fig. 9. **b, c** Angle-resolved PL intensity of LDS and CT peaks from $2L_P$ (**b**) and $3L_P$ (**c**), where the data were fitted with the square of cosine and a constant. The angle marked by a green arrow corresponds to θ_{CT-LDS} in **d**. **d** Orientation of μ_{CT} and μ_{LDS} with respect to μ_{LDS} . **e** Energy level diagram for FE-CT mixing in 2D PTCDA crystals. Whereas LDS (2.23 eV) for $1L_P$ can be considered as an unperturbed FE state (FE°), the CT state at 2.12 eV from multilayer samples is the result of FE-CT

mixing. For the symmetry convention of unperturbed CT states ($CT^{\circ,\pm}$), see the main text. **f** Scheme presenting the transition dipole moments of FE° (green arrows) and CT° (orange arrows) states for $2L_P$. Because of its crystallographic centrosymmetry about the black circle, the two neighboring $\mu_{\phi I}$ dipoles in the upper (A) and lower (B) (102)-planes are antiparallel to each other. They need to be combined in parallel for a dipole-allowed transition. Similarly, the two CT° dipoles for electron and hole transfer ($\bar{\mu}_{A^+B^-}$ and $\bar{\mu}_{A^-B^+}$) require a parallel combination for a bright state. See the main text and Supplementary Note 1 for details.

does not comply with hBN, however, its contraction induced by the cooling may reach up to 1% based on its bulk TEC⁵¹. Then, the contraction-induced redshift can be nonnegligible and may contribute to the observed redshift.

The superradiant behavior of 2D PTCDA shown in the spectral narrowing and redshift indicates that both DS excitons reside in multiple molecules, the number of which can be equated to N_c . Because N_c is inversely proportional to σ^2 ,⁵² it can be determined by comparing $1L_P$ with monomeric PTCDA dissolved in solvents as shown in Fig. 3f. For a similar dielectric environment as PTCDA crystals with a dielectric constant (ϵ) of 3.6⁵³, chloroform ($\epsilon = 4.81$) and toluene ($\epsilon = 2.38$) were used as solvents. As shown in Supplementary Fig. 8, monomeric PL spectra exhibited prominent vibrational progressions³² like $1L_P$ but with twice larger linewidth. Figure 3f shows that N_c increases from ~ 3 for 298 K to ~ 7 for 77 K. Viewing the simplicity of the model in Fig. 4, the estimated change in N_c needs to be considered semi-quantitatively: at 298 K, a given excited molecule (basis I) interacts mainly with neighboring molecules in the first shell (basis II), which leads to DS. At a lower temperature, the excitonic wavefunction becomes more delocalized beyond the first shell. Whereas N_c of ~ 4 and ~ 14 have recently been obtained at 77 K for single-basis brick-wall-type PTCDA films^{43,54}, the in-plane excitonic coupling within bulk (102) plane had been considered negligible⁹.

Out-of-plane coupling via Frenkel-CT mixing in few-layered PTCDA crystals

In this section, we show how CT excitons are modified by mixing with FE states using multilayer PTCDA crystals. CT excitons often dominate or affect the excited state of molecular aggregates with significant π - π interactions¹⁹. When CT states are energetically close to Frenkel states, their coupling can be significant enough to affect their transition energies and transition dipoles. Using momentum-resolved electronic energy loss spectroscopy, for example, Knupfer et al.⁵⁵ observed an energy-dispersive state from PTCDA crystals and derived the presence

of Frenkel-CT coupling. Whereas mixing-induced energetic variation is known for some other representative systems^{21,56}, the effects on transition dipoles have not been directly observed⁹. In this regard, thickness-controlled 2D PTCDA is a good model system to unravel the progression of Frenkel-CT mixing. Previous studies^{9,20,36} established that π - π interactions are so dominant that bulk PTCDA crystals can be viewed as a non-interacting assembly of 1D π -stacked PTCDA columns (Fig. 1d). Figure 5a shows the polarized PL spectra obtained for various thickness at 77 K. Unlike $1L_P$, thicker crystals exhibited a few broad bands including CT_{high} and CT_{low} , which are located at slightly higher energies than 298 K (see Supplementary Fig. 9 for complete angle-resolved PL spectra for $1L_P$ - $6L_P$). We note that the 0-0 emission, mostly originating from LDS at 77 K (Supplementary Fig. 9), is still preserved in multilayers, whereas the other vibronic bands are not discernible because of the intense CT emissions. As shown in Supplementary Fig. 9, the LDS emission of multilayers is also plane-polarized. This fact suggests that the 0-0 emission of multilayers originates from FEs localized at the surface layers⁵⁷ and subsequently not coupled to CT states. In contrast, the CT emissions exhibited a non-Malus behavior with distinct dependence on thickness. As shown in Fig. 5b, c and Supplementary Fig. 9c, the polar graphs of the CT peaks for 2- $3L_P$ are elliptical unlike that of LDS, which suggests that each CT peak consists of transitions from multiple states. A similar observation could be made for $2L_P$ - $6L_P$ samples (Supplementary Fig. 9). Remarkably, the transition dipole moments (μ_{CT}) of CT states approach μ_{LDS} in orientation with an increasing thickness (Supplementary Fig. 9). Assuming that μ_{CT} is aligned along the major axis of ellipses, the angle (θ_{CT-LDS}) between μ_{CT} and μ_{LDS} was determined (Fig. 5d): θ_{CT-LDS} decreased from 67° ($2L$) to 19° ($6L$).

As depicted in Fig. 5e, the thickness-dependent reorientation of μ_{CT} is attributed to the varying degree in Frenkel-CT mixing. For qualitative understanding, we adapted a perturbative mixing model^{12,58} to multilayer PTCDA crystals as given in Supplementary Note 1. In essence, observed CT states are viewed as a mixed state of

unperturbed CT (CT^0) and FE states (Fig. 5e), and can be described in a perturbation approach¹². For π -stacked dimers representing $2L_p$ shown in Fig. 5f, the mixing generates symmetric (+) and antisymmetric (−) wavefunctions (Equation S3 of Supplementary Note 1). Whereas the transition dipole moment (μ_{CT^+}) of the former vanishes because of symmetry, that (μ_{CT^-}) of the latter is modified from μ_{CT^0} by $\sqrt{2}(\kappa-\lambda)\mu_{\text{FE}^0}$, where κ and λ can be related to hole and electron transfer integrals, respectively⁵⁸. When expanded to n -mers for nL_p , the degree of FE-CT mixing may decrease because of the increasing energy difference between two constituent unperturbed states (Supplementary Note 1). This suggests that the contribution of FE^0 to CT state decreases with increasing thickness, which is schematically depicted in Supplementary Fig. 10a: For $1L_p$, μ_{LDS} , μ_{UDS} are formed orthogonal (left). With an additional layer, μ_{CT^0} aligned along \mathbf{n} axis (3D description is given in Supplementary Fig. 11) is modified by μ_{LDS} and mixed into μ_{CT} (magenta arrow; middle). For thicker layers (right), μ_{CT} is reoriented further towards \mathbf{n} axis because of the decreased Frenkel contribution, which is consistent with the observation in Fig. 5d. One might consider the opposite case, where the contribution of FE^0 rises with the increasing thickness (Supplementary Note 1). As depicted in Supplementary Fig. 10b, μ_{CT} will eventually reorient and become more aligned with μ_{LDS} for thick layers.

We note that the model analysis not only supports the experimental observation in Fig. 5d but also provides valuable insight into the nature of the Frenkel-CT mixing. Specifically, the current results visualized the orientational progression of Frenkel-CT mixing by mapping transition dipoles with respect to crystallographic axes, which is unprecedented to our knowledge. It is also notable that the experimental $\theta_{\text{CT-LDS}}$ approached its theoretical limit of -21.5° (Supplementary Fig. 10a) with increasing thickness to 6 L. This sets a rough thickness limit for the bulk behavior in regard to FE-CT mixing. Finally, thickness-dependent mixing can also be utilized in modulating exciton transport. As predicted for π -stacked dimer systems⁵⁹, the mobility of exciton is governed by the sum of long-range Coulomb and short-range CT couplings, the latter of which is highly sensitive to the detailed geometry of intermolecular stacking. In addition to the geometric manipulation of the short-range coupling⁵⁹, the control over FE-CT mixing suggested in the current work will enable novel functions and applications in various transport devices.

In this work, we described the spatial evolution of the intralayer and interlayer excitonic couplings in 2D PTCDA crystals using polarization-resolved variable-temperature spectroscopies. 2D PTCDA grown on hBN crystals by physical vapor deposition enabled fine controls over the thickness and crystallographic orientation. Electron diffractograms combined with polarized spectra led to the crystallographic details including molecular orientations of two herringbone-arranged bases. For $1L$, the 0-0 emission pair Davydov-split by Kasha-type coupling exhibited a remarkable energy inversion with decreasing temperature, which favors in-plane delocalization of the Frenkel exciton pair. With increasing thickness, CT excitons developed in the out-of-plane direction along π - π stacks. Notably, the transition dipoles of CT excitons underwent in-plane reorientation with increasing thickness, which was successfully explained with a Frenkel-CT mixing model. This work will lead to a deeper understanding of molecular excitons bound in low-dimensional organic materials and thus contribute to the better design of molecular structures with novel functions.

Methods

Growth of 2D PTCDA crystals

Mono- and few-layer PTCDA crystals were grown on high-quality inorganic 2D crystals by the self-limited epitaxy²³. Briefly, few-layer hBN and graphene were mechanically exfoliated on amorphous quartz and 285 nm SiO_2/Si substrates from hBN powder (Momentive Performance Materials) and natural graphite (NGS Naturgraphite GmbH).

PTCDA powder (TCI, >98%) and exfoliated samples were placed at the center and downstream of a tube furnace (ThermoFisher, Lindberg/Blue M), respectively. After the quartz tube was purged with a high-purity Ar gas for 30 min at 500 mL/min, the flow rate was reduced to 100 mL/min. Subsequently, the tube was heated to 330 °C at a rate of $-22^\circ\text{C}/\text{min}$ and the temperature was maintained for 15–30 min. Sublimated PTCDA molecules were found to deposit as 2D crystals on hBN and graphene. The average thickness was controlled by varying the deposition time and location within the tube.

PL spectroscopy

The employed micro-spectroscopy setup has been described elsewhere⁶⁰. Briefly, solid-state laser beams of 457.8 and 514.3 nm (Cobolt, Twist, and Fandango) were focused onto samples within a spot size of $-1\ \mu\text{m}$ using a microscope objective ($\times 40$, NA = 0.60). The signals were collected using a CCD camera (Princeton Instruments, PyLon) with a spectrometer (Princeton Instruments, SP2300). All measurements were performed in the ambient conditions unless noted otherwise. The average power was maintained below $2\ \mu\text{W}$ to avoid unwanted photoinduced degradation.

Temperature-dependent PL spectroscopy

A tunable pulsed source (Coherent, Chameleon Ultra II and Compact OPO) was used for variable-temperature PL measurements. Excitation beams of 515 nm were focused with an objective ($\times 50$, NA = 0.55) onto a $1\text{-}\mu\text{m}$ focal spot on samples. The light source was operated at a repetition rate of 80 MHz generating pulses with 140-fs duration. Samples placed in a liquid- N_2 cryostat (Linkam, HFS600E-PB4) could be cooled down to 77 K. PL signals were collected by a Czerny-Turner spectrometer (Andor, SR303i) equipped with an EMCCD camera (Andor, DU971P). For polarization-resolved experiments, an analyzing polarizer was placed in front of the spectrometer to select the polarization component parallel to that of the plane-polarized excitation beam. The polarization vector of the excitation beam could be rotated within the sample plane by rotating an achromatic half-wave plate, which was mounted on a rotational stage (Thorlabs, KPRM1E/M) and placed between the objective and tube lens. The average power was maintained below $0.2\ \mu\text{W}$ to avoid unwanted photoinduced degradation.

Optical contrast and differential reflectance

Optical absorption of 2D PTCDA on transparent substrates could be measured using its differential reflectance (DR)³⁵, defined as $(R - R_0)/R_0$, where R and R_0 are the spectral reflectance of sample and bare substrate, respectively. Optical contrast, essentially DR, was similarly determined using the green-channel signals of optical micrographs.

AFM measurements

The topographic details of samples were studied with an atomic force microscope (Park Systems, XE-70). Height and phase images were obtained in a noncontact mode using Si tips with a nominal radius of 8 nm (MicroMasch, NSC-15).

TEM sample preparation and measurements

PTCDA on 2D crystals (hBN or graphene) was covered with few-layer graphene flakes before transferring to TEM grids. Then, the resulting samples of graphene/PTCDA/hBN (or graphene)/ SiO_2/Si were overlaid with polydimethylsiloxane (PDMS) film. When soaked in ethanol/DI water mixtures (ethanol 50%, DI water 50%) for 2 h, the 2D hetero layers of the samples were released from SiO_2/Si substrates and transferred to the PDMS film. The heterostructures on PDMS were dried under ambient conditions and transferred again to holey SiN TEM grids (Norcada Inc.) by stamping via a micromanipulator under optical microscope observation. SAED acquisition was performed with a JEOL ARM 200F equipped with image and probe aberration

correctors operated at 80 kV. SAED simulations were performed by CrystalDiffract (CrystalMaker Software Ltd.).

Data availability

The authors declare that all data supporting the findings of this study are available within the paper and its supplementary information file or available from the corresponding author upon request.

References

- Hedley, G. J., Ruseckas, A. & Samuel, I. D. Light harvesting for organic photovoltaics. *Chem. Rev.* **117**, 796–837 (2017).
- Cui, Y. et al. Over 16% efficiency organic photovoltaic cells enabled by a chlorinated acceptor with increased open-circuit voltages. *Nat. Commun.* **10**, 2515 (2019).
- Uoyama, H., Goushi, K., Shizu, K., Nomura, H. & Adachi, C. Highly efficient organic light-emitting diodes from delayed fluorescence. *Nature* **492**, 234–238 (2012).
- Chen, Q., Rada, T., Bitzer, T. & Richardson, N. V. Growth of PTCDA crystals on H: Si(111) surfaces. *Surf. Sci.* **547**, 385–393 (2003).
- Davydov, A. S. The theory of molecular excitons. *Sov. Phys. Usp.* **7**, 145 (1964).
- Hochstrasser, R. M. & Kasha, M. Application of the exciton model to mono-molecular lamellar systems. *Photochem. Photobiol.* **3**, 317–331 (1964).
- Dicke, R. H. Coherence in spontaneous radiation processes. *Phys. Rev.* **93**, 99 (1954).
- Benedict, M. G.; Ermolaev, A. M.; Malyshev, V.; Sokolov, I.; Trifonov, E. D. *Super-Radiance: Multiatomic Coherent Emission* (CRC Press, Boca Raton, 2018).
- Hoffmann, M. et al. The lowest energy frenkel and charge-transfer excitons in quasi-one-dimensional structures: application to MePTCDI and PTCDA crystals. *Chem. Phys.* **258**, 73–96 (2000).
- Singh, S., Jones, W., Siebrand, W., Stoicheff, B. & Schneider, W. Laser generation of excitons and fluorescence in anthracene crystals. *J. Chem. Phys.* **42**, 330–342 (1965).
- Kasha, M. Energy transfer mechanisms and the molecular exciton model for molecular aggregates. *Radiat. Res.* **20**, 55–70 (1963).
- Harcourt, R. D., Scholes, G. D. & Ghiggino, K. P. Rate expressions for excitation transfer. ii. electronic considerations of direct and through-configuration exciton resonance interactions. *J. Chem. Phys.* **101**, 10521–10525 (1994).
- Jackson, J. D. *Classical electrodynamics* (Wiley, New York, 1999).
- Dexter, D. L. A theory of sensitized luminescence in solids. *J. Chem. Phys.* **21**, 836–850 (1953).
- Hestand, N. J. & Spano, F. C. Molecular aggregate photophysics beyond the kasha model: novel design principles for organic materials. *Acc. Chem. Res.* **50**, 341–350 (2017).
- Hestand, N. J. & Spano, F. C. Interference between coulombic and CT-mediated couplings in molecular aggregates: H-to J-aggregate transformation in perylene-based π -stacks. *J. Chem. Phys.* **143**, 244707 (2015).
- Gisslén, L. & Scholz, R. Crystalochromy of perylene pigments: interference between frenkel excitons and charge-transfer states. *Phys. Rev. B* **80**, 115309 (2009).
- Monahan, N. & Zhu, X. Y. Charge transfer-mediated singlet fission. *Annu. Rev. Phys. Chem.* **66**, 601–618 (2015).
- Hestand, N. J. & Spano, F. C. Expanded theory of H- and J-molecular aggregates: the effects of vibronic coupling and intermolecular charge transfer. *Chem. Rev.* **118**, 7069–7163 (2018).
- Zhao, H. et al. Strong optical response and light emission from a monolayer molecular crystal. *Nat. Commun.* **10**, 1–9 (2019).
- Yamagata, H. et al. The nature of singlet excitons in oligoacene molecular crystals. *J. Chem. Phys.* **134**, 204703 (2011).
- Zhou, J. et al. Magic-angle stacking and strong intermolecular π - π interaction in A perylene bisimide crystal: an approach for efficient near-infrared (NIR) emission and high electron mobility. *J. Phys. Chem.* **9**, 596–600 (2018).
- Wu, B. et al. Precise, self-limited epitaxy of ultrathin organic semiconductors and heterojunctions tailored by van der Waals Interactions. *Nano Lett.* **16**, 3754–3759 (2016).
- Koo, S. et al. Extraordinary photostability and davydov splitting in BN-sandwiched single-layer tetracene molecular crystals. *Nano Lett.* **21**, 6600–6608 (2021).
- Shin, J. Y. et al. Aromaticity and photophysical properties of various topology-controlled expanded porphyrins. *Chem. Soc. Rev.* **39**, 2751–2767 (2010).
- Kim, K., Santos, E. J., Lee, T. H., Nishi, Y. & Bao, Z. Epitaxially grown strained pentacene thin film on graphene membrane. *Small* **11**, 2037–2043 (2015).
- Heinemeyer, U. et al. Exciton-phonon coupling in diindenoperylene thin films. *Phys. Rev. B* **78**, 085210 (2008).
- Raja, A. et al. Coulomb engineering of the bandgap and excitons in two-dimensional materials. *Nat. Commun.* **8**, 15251 (2017).
- Ogawa, T., Kuwamoto, K., Isoda, S., Kobayashi, T. & Karl, N. 3,4:9,10-perylenetetracarboxylic dianhydride (PTCDA) by electron crystallography. *Acta Crystallogr. Sect. B Struct. Sci.* **55**, 123–130 (1999).
- Möbus, M., Karl, N. & Kobayashi, T. Structure of perylene-tetracarboxylic-dianhydride thin films on alkali halide crystal substrates. *J. Cryst. Growth* **116**, 495–504 (1992).
- Schneider, M., Umbach, E. & Sokolowski, M. Growth-dependent optical properties of 3,4,9,10-perylenetetracarboxylicacid-dianhydride (PTCDA) films on Ag(111). *Chem. Phys.* **325**, 185–192 (2006).
- Bulović, V., Burrows, P., Forrest, S., Cronin, J. & Thompson, M. Study of localized and extended excitons in 3, 4, 9, 10-perylenetetracarboxylic dianhydride (PTCDA) I. Spectroscopic properties of thin films and solutions. *Chem. Phys.* **210**, 1–12 (1996).
- Wagner, H., DeSilva, A. & Kampen, T. U. Exciton emission in PTCDA films and PTCDA/Alq₃ multilayers. *Phys. Rev. B* **70**, 235201 (2004).
- Chen, W. et al. Molecular orientation of 3, 4, 9, 10-perylene-tetracarboxylic-dianhydride thin films at organic heterojunction interfaces. *Appl. Phys. Lett.* **91**, 114102 (2007).
- Mak, K. F. et al. Measurement of the optical conductivity of graphene. *Phys. Rev. Lett.* **101**, 196405 (2008).
- Mazur, G., Petelenz, P. & Slawik, M. Theoretical calculations of the electroabsorption spectra of perylenetetracarboxylic dianhydride. *J. Chem. Phys.* **118**, 1423–1432 (2003).
- Gangilenka, V. R. et al. Exciton emission in PTCDA thin films under uniaxial pressure. *Phys. Rev. B* **77**, 115206 (2008).
- Alonso, M. I., Garriga, M., Karl, N., Osso, J. O. & Schreiber, F. Anisotropic optical properties of single crystalline PTCDA studied by spectroscopic ellipsometry. *Org. Electron.* **3**, 23–31 (2002).
- Yuan, J. et al. Invoking ultralong room temperature phosphorescence of purely organic compounds through H-aggregation engineering. *Mater. Horiz.* **6**, 1259–1264 (2019).
- Cong, K. K. et al. Dicke superradiance in solids. *J. Opt. Soc. Am. B* **33**, C80–C101 (2016).
- Spano, F. C. Emission from aggregates of oligo-phenylene vinylenes: a recipe for superradiant H-aggregates. *Chem. Phys. Lett.* **331**, 7–13 (2000).
- Lim, S. H., Bjorklund, T. G., Spano, F. C. & Bardeen, C. J. Exciton delocalization and superradiance in tetracene thin films and nanoaggregates. *Phys. Rev. Lett.* **92**, 107402 (2004).
- Muller, M., Paulheim, A., Einfeld, A. & Sokolowski, M. Finite size line broadening and superradiance of optical transitions in two dimensional long-range ordered molecular aggregates. *J. Chem. Phys.* **139**, 044302 (2013).
- Putnam, R. E. Jr & Raikh, M. E. Renormalization of the 3D exciton spectrum by the disorder. *Solid State Commun.* **340**, 114522 (2021).

45. Walczak, P. B., Eisfeld, A. & Briggs, J. S. Exchange narrowing of the J band of molecular dye aggregates. *J. Chem. Phys.* **128**, 044505 (2008).
46. Chuang, C. et al. Generalized Kasha's model: T-dependent spectroscopy reveals short-range structures of 2d excitonic systems. *Chem* **5**, 3135–3150 (2019).
47. Alvertis, A. M. et al. Impact of exciton delocalization on exciton-vibration interactions in organic semiconductors. *Phys. Rev. B* **102**, 081122 (2020).
48. Cai, Q. R. et al. High thermal conductivity of high-quality monolayer boron nitride and its thermal expansion. *Sci. Adv.* **5**, eaav0129 (2019).
49. Seremetis, L. et al. Thermomechanical response of supported hexagonal boron nitride sheets of various thicknesses. *J. Phys. Chem. C* **124**, 12134–12143 (2020).
50. Collocott, S. J. & White, G. K. Heat-capacity and thermal-expansion of zerodur and zerodur-M at low-temperatures. *Cryogenics* **31**, 102–104 (1991).
51. Krause, B. Growth and structure of the organic molecule PTCDA on Ag (111). PhD Thesis, University of Stuttgart, Stuttgart, Germany (2002).
52. Meinardi, F., Cerminara, M., Sassella, A., Bonifacio, R. & Tubino, R. Superradiance in molecular H aggregates. *Phys. Rev. Lett.* **91**, 247401 (2003).
53. Schwenn, P. E., Burn, P. L. & Powell, B. J. Calculation of solid state molecular ionisation energies and electron affinities for organic semiconductors. *Org. Electron.* **12**, 394–403 (2011).
54. Eisfeld, A., Marquardt, C., Paulheim, A. & Sokolowski, M. Super-radiance from two dimensional brick-wall aggregates of dye molecules: the role of size and shape for the temperature dependence. *Phys. Rev. Lett.* **119**, 097402 (2017).
55. Knupfer, M., Schwieger, T., Fink, J., Leo, K. & Hoffmann, M. Excitons in quasi-one-dimensional organic crystals. *Phys. Rev. B* **66**, 035208 (2002).
56. Austin, A. et al. Enhanced Davydov splitting in crystals of a perylene diimide derivative. *J. Phys. Chem. Lett.* **8**, 1118–1123 (2017).
57. Agranovich, V. M., Atanasov, R. D. & Bassani, G. F. Excitons in organic multiple quantum-well structures. *Chem. Phys. Lett.* **199**, 621–624 (1992).
58. Yamagata, H., Pochas, C. M. & Spano, F. C. Designing J-and H-aggregates through wave function overlap engineering: applications to poly (3-hexylthiophene). *J. Phys. Chem. B* **116**, 14494–14503 (2012).
59. Hestand, N. J., Tempelaar, R., Knoester, J., Jansen, T. L. C. & Spano, F. C. Exciton mobility control through sub-angstrom packing modifications in molecular crystals. *Phys. Rev. B* **91**, 195315 (2015).
60. Park, K., Kang, H., Koo, S., Lee, D. & Ryu, S. Redox-governed charge doping dictated by interfacial diffusion in two-dimensional materials. *Nat. Commun.* **10**, 4931 (2019).
61. Gisslén, L. M. Influence of Frenkel excitons and charge transfer states on the spectroscopic properties of organic molecular crystals. Ph.D. Thesis, Technical University of Munich, Munich, Germany (2010).

Acknowledgements

S.R. acknowledges the financial support from the Samsung Research Funding Center of Samsung Electronics (Project Number SSTF-BA1702-08), National Research Foundation of Korea (NRF-2020R1A2C2004865 and NRF-2022R1A4A1033247) and Samsung Electronics Co., Ltd (IO201215-08191-01).

Author contributions

S.R. conceived the project. D.K. and S.R. designed the experiments. D.K. prepared samples, performed spectroscopy experiments, and analyzed the data. J.P., J.L., and H.C.C. established the growth method of PTCDA crystals. S.L. and K.K. conducted the SAED measurements and analysis. D.K. and S.R. wrote the manuscript with contributions from all authors.

Competing interests

The authors declare no competing interests.

Additional information

Supplementary information The online version contains supplementary material available at <https://doi.org/10.1038/s41467-023-38438-0>.

Correspondence and requests for materials should be addressed to Sunmin Ryu.

Peer review information *Nature Communications* thanks the anonymous reviewer(s) for their contribution to the peer review of this work.

Reprints and permissions information is available at <http://www.nature.com/reprints>

Publisher's note Springer Nature remains neutral with regard to jurisdictional claims in published maps and institutional affiliations.

Open Access This article is licensed under a Creative Commons Attribution 4.0 International License, which permits use, sharing, adaptation, distribution and reproduction in any medium or format, as long as you give appropriate credit to the original author(s) and the source, provide a link to the Creative Commons license, and indicate if changes were made. The images or other third party material in this article are included in the article's Creative Commons license, unless indicated otherwise in a credit line to the material. If material is not included in the article's Creative Commons license and your intended use is not permitted by statutory regulation or exceeds the permitted use, you will need to obtain permission directly from the copyright holder. To view a copy of this license, visit <http://creativecommons.org/licenses/by/4.0/>.

© The Author(s) 2023, corrected publication 2023